Ultramicroscopy 282 (2026) 114305

Contents lists available at ScienceDirect

Ultramicroscopy

journal homepage: www.elsevier.com/locate/ultramic

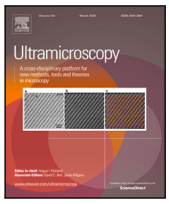

Fabrication and characterization of boron-terminated tetravacancies in monolayer hBN using STEM, EELS and electron ptychography☆

Dana O. Byrne [a,b,c,*], Stephanie M. Ribet [c], Demie Kepaptsoglou [d,e], Quentin M. Ramasse [d,f], Colin Ophus [g], Frances I. Allen [b,c,h,*]

[a] Department of Chemistry, University of California, Berkeley, CA, 94720, USA
[b] Department of Materials Science and Engineering, University of California, Berkeley, CA, 94720, USA
[c] Molecular Foundry, Lawrence Berkeley National Laboratory, Berkeley, CA, 94720, USA
[d] SuperSTEM Laboratory, SciTech Daresbury Campus, Daresbury, WA4 4AD, UK
[e] School of Physics, Engineering and Technology & JEOL Nanocentre, University of York, Heslington, YO10 5DD, UK
[f] School of Chemical and Process Engineering & School of Physics and Astronomy, University of Leeds, LS2 9JT, UK
[g] Department of Materials Science and Engineering, Stanford University, CA, 94305, USA
[h] California Institute for Quantitative Biosciences, University of California, Berkeley, CA, 94720, USA

ARTICLE INFO

Keywords:
2D hBN
Defect engineering
Nanopores
STEM
EELS
Ptychography

ABSTRACT

Tetravacancies in monolayer hexagonal boron nitride (hBN) with consistent edge termination (boron or nitrogen) form triangular nanopores with electrostatic potentials that can be leveraged for applications such as selective ion transport and neuromorphic computing. In order to quantitatively predict the properties of these structures, an atomic-level understanding of their local electronic and chemical environments is required. Moreover, robust methods for their precision manufacture are needed. Here we use electron irradiation in a scanning transmission electron microscope (STEM) at a high dose rate to drive the formation of boron-terminated tetravacancies in monolayer hBN. Characterization of the defects is achieved using aberration-corrected STEM, monochromated electron energy-loss spectroscopy (EELS), and electron ptychography. Z-contrast in STEM and chemical fingerprinting by core-loss EELS enable identification of the edge terminations, while electron ptychography gives insight into structural relaxation of the tetravacancies and provides evidence of enhanced electron density around the defect perimeters indicative of bonding effects.

1. Introduction

With the advent of low-voltage aberration-corrected scanning/transmission electron microscopy (S/TEM), atomic-resolution imaging of the delicate monolayers of 2D materials has become possible [1,2]. However, it was soon discovered that significant re-arrangement and removal of atoms from the lattice can still occur [3], even at beam energies well below elastic knock-on thresholds, due to inelastic electron scattering effects such as radiolysis [4]. Although sample damage during imaging typically needs to be minimized, there is also interest in leveraging this damage in a controlled way for defect engineering on the single atom level [5–9].

The first high-resolution studies of electron-irradiation-induced atomic rearrangements in a 2D material focused on graphene, reporting the formation of holes with the so-called zigzag and armchair edges [3]. Soon after, experiments with 2D hexagonal boron nitride (hBN) were conducted, demonstrating the formation of perfect triangular-shaped multi-atom vacancy defects under the electron beam [10–12]. The regular geometric shape is due to preferential ejection of one atomic species over the other, which drives the expanding defect to follow the triangular sublattice of either element.

While initial reports of triangular vacancy defect growth in 2D hBN determined preferential boron atom ejection (creating nitrogen-terminated defects) [10,12,13], other studies have reported preferential nitrogen atom ejection [14], or even, no particular atomic preference at all [15–18]. The key parameters affecting the energetics of the defect expansion process are beam energy, sample temperature, electron dose rate, and the presence (or lack) of residual species in the vacuum. Clearly, these factors need to be thoroughly understood in order for precision engineering of defects in the electron microscope to become a predictable and reliable enterprise.

Tetravacancies in 2D hBN with consistent edge termination (lined with either boron or nitrogen atoms) are of particular interest in membrane applications that leverage the electrostatic potential inside such

☆ This article is part of a Special issue entitled: 'FEMMS 2024' published in Ultramicroscopy.

* Corresponding authors.
E-mail addresses: dana_byrne@berkeley.edu (D.O. Byrne), francesallen@berkeley.edu (F.I. Allen).

https://doi.org/10.1016/j.ultramic.2025.114305
Received 19 April 2025; Received in revised form 18 December 2025; Accepted 24 December 2025
Available online 26 December 2025

pores. These applications include selective filtration via mechanosensitive ion transport [19] and neuromorphic computing via memristive response [20]. In order to quantitatively predict the behavior of the nanopores, their atomic, electronic and chemical structure need to be precisely known. Here, advanced electron microscopy can lead the way, using aberration-corrected STEM at low-kV for defect identification at the single atom level [21], high energy-resolution electron energy-loss spectroscopy (EELS) to probe the electronic and chemical structure of the defects [22–25], and electron ptychography for dose-efficient mapping of atom positions and properties with deep sub-Ångström resolution by quantitative phase retrieval of the electron exit wave [26,27].

In this work, we employ aberration-corrected STEM, monochromated EELS and electron ptychography to fabricate and analyze vacancy defect structures in hBN monolayers. All experiments are performed in UHV at 60 kV with the samples held at room temperature. When scanning at high dose rates, we find that boron-terminated tetravacancies are preferentially formed. The defect edge terminations are first determined based on Z-contrast in high angle annular dark-field (HAADF) STEM images, and also using chemical fingerprinting via monochromated STEM-EELS of the boron K-edge. Atom maps obtained by electron ptychography reveal distortions around the defect edges indicative of structural stabilization, although artifacts from sample charging during the scans must also be considered. The ptychographic reconstructions also show enhanced phase shifts around the defect perimeters, the potential origins of which are discussed.

2. Experimental

2.1. Preparation of hBN monolayers

Monolayer hBN, grown by chemical vapor deposition on copper (Grolltex Inc.), was transferred onto custom holey silicon nitride (SiN_x) TEM grids using a wet transfer electrochemical delamination method [28]. For this, small sections of the hBN on copper were cut out and spin-coated with 11% polymethyl methacrylate (PMMA) in anisole. The copper/hBN/PMMA films were then clipped to the anode of a two electrode system with NaCl/water electrolyte and a glassy carbon cathode. A 5 V bias was applied to generate hydrogen bubbles at the anode, which gently removes the hBN/PMMA layer from the copper. The hBN/PMMA film was washed several times in deionized water and transferred onto the custom SiN_x TEM grids. Finally, the PMMA was removed with an acetone drip.

In the experiments described here, we worked with both "pristine" regions of the hBN (native defects only) and regions that had been irradiated with helium ions to create higher densities of single atom vacancy defect seeds for subsequent expansion upon electron irradiation in STEM. The ion irradiation was performed site selectively using a Zeiss ORION NanoFab multibeam He-Ne-Ga focused ion beam microscope, using the helium ion beam in a low-dose raster [28,29]. A typical irradiation dose was 10 ions/nm^2 and the helium ion beam energy was set to 25 keV. The ion-irradiated samples were also air-annealed to remove additional hydrocarbon surface contamination that formed on those specimens and to promote the growth of larger defect structures, as described in our previous study [28].

2.2. HAADF-STEM and monochromated STEM-EELS

Electron microscopy was performed using a Nion UltraSTEM 100MC "Hermes" aberration-corrected microscope operated at 60 kV using a convergence semi-angle of 31 mrad, corresponding to ~1 Å electron probe diameter. The vacuum at the sample ranged from $\sim 1.2\times10^{-9}$ Torr to 7.8×10^{-10} Torr, depending on the time that had elapsed after sample insertion (this variation is unlikely to result in significant differences in the partial pressures of molecules contributing to chemical etching). All experiments were performed at room temperature. Defect growth was observed both during lower dose rate survey imaging and in the higher dose rate EELS (and later ptychography) acquisitions.

For the lower magnification HAADF-STEM survey imaging, typical parameters were a beam current of 6 pA, pixel dwell time of 240 µs, and scan spacing of 0.02 nm. A typical scan size was 512 × 512 pixels (field of view 10.24 nm), giving a time-averaged dose rate of 3.6×10^5 e/nm^2/s (calculated from the beam current divided by the scan area). The corresponding accumulated dose was 2.3×10^7 e/nm^2.

Most high magnification HAADF-STEM scans were acquired using a beam current of 6 pA, pixel dwell time of 4.9 ms, and scan spacing of 0.03 nm, for a series of five or more frames (see Fig. S1). The typical scan size was 50 × 50 pixels (field of view 1.5 nm), giving a time-averaged dose rate of 1.7×10^7 e/nm^2/s. The corresponding total dose for a single frame was 2.0×10^8 e/nm^2. Image series with minimal defect movement between frames were identified, manually drift corrected using DigitalMicrograph® software, and finally averaged using custom Python code to increase the signal-to-noise ratio in the final image.

In parallel with the high magnification HAADF-STEM acquisitions, an EEL spectrum was collected for every pixel in the scan using the Nion IRIS spectrometer equipped with a Dectris ELA hybrid-pixel detector. The beam current used for the EELS results shown in this paper was 30 pA, corresponding to a time-averaged dose rate of 1.1×10^8 e/nm^2/s for a 41 × 45 pixel scan. A collection angle of 44 mrad was used and the energy dispersion was 0.1 eV/channel. Here, we focus primarily on the boron K-edge.

The STEM-EELS data were analyzed using the open-source `HyperSpy` package [30] and custom Python code. This involved spatial drift correction of the frames in the spectrum image using the accompanying HAADF series, image and spectrum averaging, spatial binning, spectrum smoothing with a total variation function, and then non-negative matrix factorization (NNMF) using the `Scipy` package [31] to identify and map spectral features in the vicinity of the onset of the boron K-edge. NNMF score images were used to generate boolean masks, which allowed for spatial separation of features for spectral plotting (see Fig. S2). The final spectra presented here have been normalized to the σ^* peak of the boron K-edge (full spectral range shown in Fig. S3). All spectra were shifted in the energy axis to align with the energy-loss value of the B–N π^* peak obtained in [29]. Further boron K-edge spectra are shown in Fig. S4 and a nitrogen K-edge spectrum is shown in Fig. S5. Shifts in the energy axis did occur over the span of several hours, so the calibrations are never absolute, but internally all efforts are made to ensure spectra are comparable across datasets.

2.3. Electron ptychography

Data collection for the ptychography was also performed using the Nion UltraSTEM microscope operated at 60 kV with a probe convergence angle of 31 mrad. The detector used was a sCMOS Ronchigram camera (Hamamatsu Orca v2). Using a probe defocus value of 13 nm, 4D-STEM data were collected for every probe position in the scan, i.e. a diffraction pattern with reciprocal space co-ordinates (k_x, k_y) for every spatial position with real space co-ordinates (x, y). The beam current was 30 pA, pixel dwell time 5 ms, scan spacing 0.047 nm, and scan size 128 × 128 pixels (field of view of ~6 nm). The time-averaged dose rate was thus 5.2×10^6 e/nm^2/s. The region was scanned several times before the final acquisition, giving a total dose received by the area of $\sim 2.5\times10^9$ e/nm^2.

The ptychographic reconstruction was performed in the open-source package `py4DSTEM` [32,33]. We used a single slice stochastic gradient descent algorithm with a batch size of 4096 probe positions. The final complex object reconstruction used 100 iterations of step size 0.1 with probe position refinement. A high-pass Butterworth filter was applied to the final object. The full reconstruction is shown in Fig. S6.

The best-fit atomic positions were determined using custom Matlab code. First, we estimated the approximate atomic positions from local intensity maxima. Next, we refined the positions by fitting a

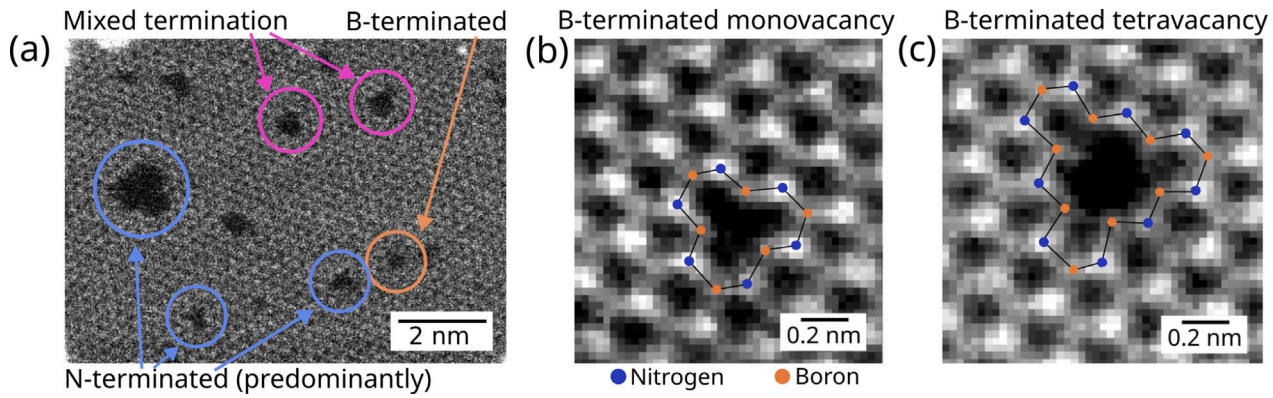

Fig. 1. (a) HAADF-STEM survey showing vacancy defects in hBN after scanning at low dose rate. A number of defects are circled to indicate those with predominantly nitrogen termination (blue), boron termination (orange), and mixed edge termination (pink). (b–c) High magnification HAADF-STEM images of a monovacancy and a tetravacancy, respectively, acquired at high dose rate with edge atom models overlaid. These defects are boron terminated. The atom models shown here give approximate atom locations only.

Gaussian distribution using nonlinear least squares. Finally, we refined the positions by fitting a Gaussian distribution after subtracting the current estimated intensity from all neighboring peaks. This last step was performed iteratively until convergence. In the reconstruction, the mean B–B distance corresponding to the bulk lattice was measured to be (2.65 ± 0.10) Å. Figure S6 shows the control region used for this measurement. Given the literature value of 2.51 Å [34], the atomic positions in the reconstruction were scaled accordingly, from which all subsequent bond length measurements were then made.

3. Results and discussion

3.1. Vacancy defects created upon scanning at low dose rate vs. high dose rate

Fig. 1 shows HAADF-STEM images of a monolayer of hBN that had been pre-treated, as described in the methods, to produce a distribution of single-atom vacancies and larger vacancy defects for subsequent manipulation and analysis in STEM. In low dose rate scans, defects with different edge terminations were observed, as seen in Fig. 1(a). Most of these defects were small (< 24 atom vacancies) and include triangular defects with either nitrogen or boron atom termination, as well as hexagonal defects, which inherently feature alternating boron- and nitrogen-terminated edges. Edge termination was assigned based on Z-contrast, with nitrogen atoms appearing brighter than boron atoms. This contrast was used to identify the triangular nitrogen and boron atom sublattices, from which the edge termination of the geometric defects could be determined. Nitrogen- vs. boron-terminated triangular defects point in opposite directions.

Even though the imaging dose rates and total doses used for the survey images were relatively low ($\sim 10^5$ e/nm^2/s and $\sim 10^7$ e/nm^2, respectively), defect growth and movement between frames was observed. This illustrates the challenge of non-invasive imaging defects in beam-sensitive materials, while also demonstrating the capability to use the electron beam for intentional atom manipulation. In particular the larger defects are more unstable and thus expand more quickly, such as the larger defect highlighted on the left hand side of Fig. 1(a). This defect is essentially a nitrogen-terminated triangle with truncated corners terminated with boron. Overall we infer a preference for nitrogen-terminated growth in the low-dose scans, although we note that defects with no obvious geometric preference also formed.

In higher dose rate scans ($\sim 10^7$ e/nm^2/s), boron-terminated defects were predominantly observed. Examples are given in the HAADF images of Figs. 1(b) and (c), which show a boron-terminated monovacancy and tetravacancy, respectively. While the monovacancy may have already been present, the tetravacancy formed upon the high dose rate scanning. Out of 62 high dose rate scans in which defect edge termination could be clearly identified (each scan comprising multiple frames), 44 scans had at least one frame with a boron-terminated defect, while only 16 scans had at least one frame with a nitrogen-terminated defect. We note that identification of stable defect states was often challenging, since defects were typically very mobile during scanning, growing and/or changing shape from one frame to the next (see Fig. S1). However, in several scans taken at dose rates as high as 10^8 e/nm^2/s, even greater preference for boron vs. nitrogen termination was indicated.

Our results thus reveal a preference for nitrogen atom ejection at the higher dose rates, resulting in the boron-terminated defects observed. Of these, the tetravacancies were the most stable during the high dose rate scans. Interestingly, in subsequent survey imaging at the lower dose rates, some of these boron-terminated tetravacancies appeared to have reconfigured, or may have been filled with carbon atoms [35]. This could have occurred when the beam was blanked, or during the low dose rate scanning. Such reconfiguration supports the conclusion that different damage mechanisms and kinetics are at play depending on the imaging conditions.

3.2. Probing boron-terminated tetravacancies using core-loss STEM-EELS

STEM-EELS core-loss spectrum imaging was used to probe the defects, as shown in Fig. 2. Since these were also high dose rate acquisitions (taken in parallel with the high-magnification HAADF images discussed above), boron-termination was prevalent. Fig. 2(a) shows boron K-edge EELS results for a boron-terminated tetravacancy, focusing on the π^* region of the spectrum. The corresponding HAADF image is shown in Fig. 2(b). A distinct pre-peak feature associated with the boron-terminated defect is found (marked with the dashed red line). This feature has been identified previously and analyzed in more detail by Cretu et al. [14] and Gao et al. [36]. Here, we use NNMF to identify the pre-peak in our dataset and to determine its spatial distribution. The resulting score map is shown in Fig. 2(c). The bright green pixels indicate the presence of the pre-peak, which maps to the defect perimeter. This map was then used to create a mask to generate the "defect" and "bulk monolayer" spectra shown in Fig. 2(a). More detail on the NNMF analysis can be found in Fig. S2, with further examples of the boron K-edge pre-peak from other datasets shown in Fig. S4.

The pre-peak in the boron K-edge spectrum is essentially a chemical shift of the bulk π^* peak due to the dangling bonds on the undercoordinated boron atoms, serving as a fingerprint for the boron-terminated tetravacancy [14,36]. Thus, both Z-contrast in HAADF-STEM and the pre-peak in the boron K-edge EELS can be used to determine the edge

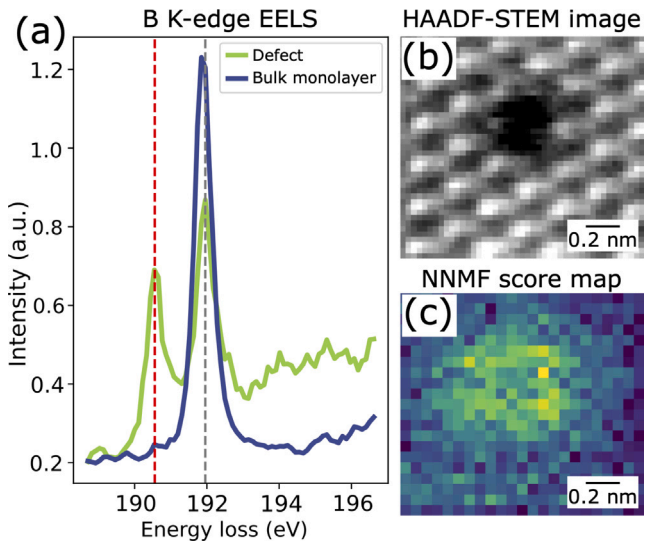

Fig. 2. (a) Boron K-edge EEL spectrum imaging of a boron-terminated tetravacancy comparing the signal from the defect vs. the bulk monolayer, normalized to the σ^* peak (see Fig. S3). The gray dashed line marks the energy of the π^* peak from the bulk monolayer while the red dashed line indicates the energy at which a shifted pre-peak appears. (b) Corresponding HAADF-STEM image. (c) Score map for the pre-peak feature obtained by NNMF decomposition of the spectrum image. This map was used to create a mask to extract the individual spectra shown in (a) (see Fig. S2).

termination of the defect. The fact that the non-shifted π^* peak is also detected at the defect site is due to signal delocalization from the neighboring fully-coordinated boron atoms [37].

Since near-edge structure is mainly affected by bonding with nearest neighbors, a distinct signature in the nitrogen K-edge is not expected for boron-terminated tetravacancies, as all nitrogen atoms remain fully coordinated. Any change in the nitrogen K-edge from second neighbor sites would be extremely subtle and unlikely to be observed in our experimental conditions due to the relative lack of stability of the structure. Consistent with this expectation, no measurable change in the nitrogen K-edge was detected (see Fig. S5). Conversely, for nitrogen-terminated tetravacancies, one would anticipate the appearance of a pre-peak in the nitrogen K-edge, with minimal change in the boron K-edge [36,38]. However, because boron-terminated tetravacancies predominated in our STEM–EELS measurements, a detailed spectral analysis of the opposite termination was not feasible in the present work.

3.3. Probing boron-terminated tetravacancies using electron ptychography

To further probe the structure and bonding of the boron-terminated tetravacancies, we performed electron ptychography. Fig. 3(a) summarizes the results, showing ptychographic reconstructions of three separate tetravacancies with atom map overlays. The atomic coordinates for the maps were determined using an iterative Gaussian distribution fitting method, as described in the methods.

While one of the strengths of ptychography is its dose efficiency, we purposefully used higher doses for our acquisitions. As discussed previously, higher dose rates appear to drive the defect growth towards boron termination. Indeed, all of the tetravacancies observed in the ptychographic reconstructions are inferred to be boron terminated. We note that the more uniform contrast around the defect perimeters (discussed further below) introduces some ambiguity in atomic species assignment, however, by referencing the surrounding bulk lattice and by comparison with the high dose rate HAADF and EELS measurements, boron termination is strongly supported. The shape and edge composition of the tetravacancies is visualized more closely via the defect models shown in Fig. 3(b).

Dashed lines in Fig. 3(b) mark the distances between the boron atoms in the corner regions of the triangular tetravacancies. The average B–B distance from these measurements is (1.9 ± 0.1) Å, which is significantly shorter than the B–B distance in the pristine lattice of 2.5 Å. Similar contraction has been revealed by HAADF-STEM imaging of boron-terminated tetravacancies elsewhere [15] and has been attributed to direct bonding between the boron atoms in the corners upon structural relaxation of the defect [15,39]. We note that lattice distortion is also observed more broadly in the reconstruction, as shown in Fig. S6 (full field of view, encompassing all three defects analyzed in Fig. 3). The observed distortion may be an artifact caused by charging during the scan and could account for the more pronounced deformation of Defect #2.

An intriguing feature revealed by the ptychography is enhanced brightness around the defect perimeters. The enhancement is emphasized further in the colorized reconstruction images shown in Fig. S7 and is particularly marked for Defect #1, where the nine atoms forming the ring-like structure (highlighted in the defect model) are the brightest. Since Z-contrast in the HAADF-STEM surveys did not show this effect, we rule out dopant species as the cause. In addition, since both the boron and nitrogen atoms exhibit the increased brightness, we conclude that the effect is not specific to a single atomic species. A possible explanation may be that we are observing the effect of atom movement due to instability at the open edges. However, it seems more likely that we are in fact mapping charge redistribution due to bonding, as recently investigated by electron ptychography of sulfur vacancies in monolayer molybdenum disulfide [40]. The possibility to use electron ptychography to map bonding around defects in low-Z 2D materials such as hBN is a tantalizing prospect.

3.4. Contextual analysis of experimental parameters affecting defect growth energetics

As mentioned in the Introduction, various experimental parameters can influence the energetics of defect growth and hence steer the final defect shape and edge termination. Table 1 illustrates this point, comparing our observation of boron-atom termination under high dose rate STEM exposure with trends reported in prior studies. The table is organized according to defect shape: triangle, hexagon, parallelogram and circular. Results from both STEM and TEM experiments are given. In the STEM experiments, Z-contrast in HAADF means that boron and nitrogen can be easily differentiated, making edge terminations straightforward to assign. This is not the case in TEM mode, where differences in phase contrast between the two elements are much more subtle. Therefore, for the TEM experiments that report triangular defects (shapes that have edges terminated entirely by boron or nitrogen atoms), only those cases are listed in which further analysis was performed to determine the edge composition. The beam acceleration potentials used tend to be low (usually $\leq$80 kV) to avoid excessive defect growth due to knock-on (elastic) collisions.

Most studies have reported triangular defects that are nitrogen terminated, primarily in experiments performed at room temperature [10,12–15], but also under cryogenic conditions and at elevated temperatures up to 500 °C [15]. The majority of these studies were conducted in TEM mode. However, in a particular set of TEM experiments performed at 500 °C, a fraction of the triangular defects tended towards boron termination [14]. In the same work, the authors reported that under STEM imaging at this temperature, exclusively boron-terminated defects were formed. This marks a distinct shift from preferential boron atom removal (i.e. nitrogen termination) at lower temperatures to preferential nitrogen atom removal (boron termination) at the higher temperature.

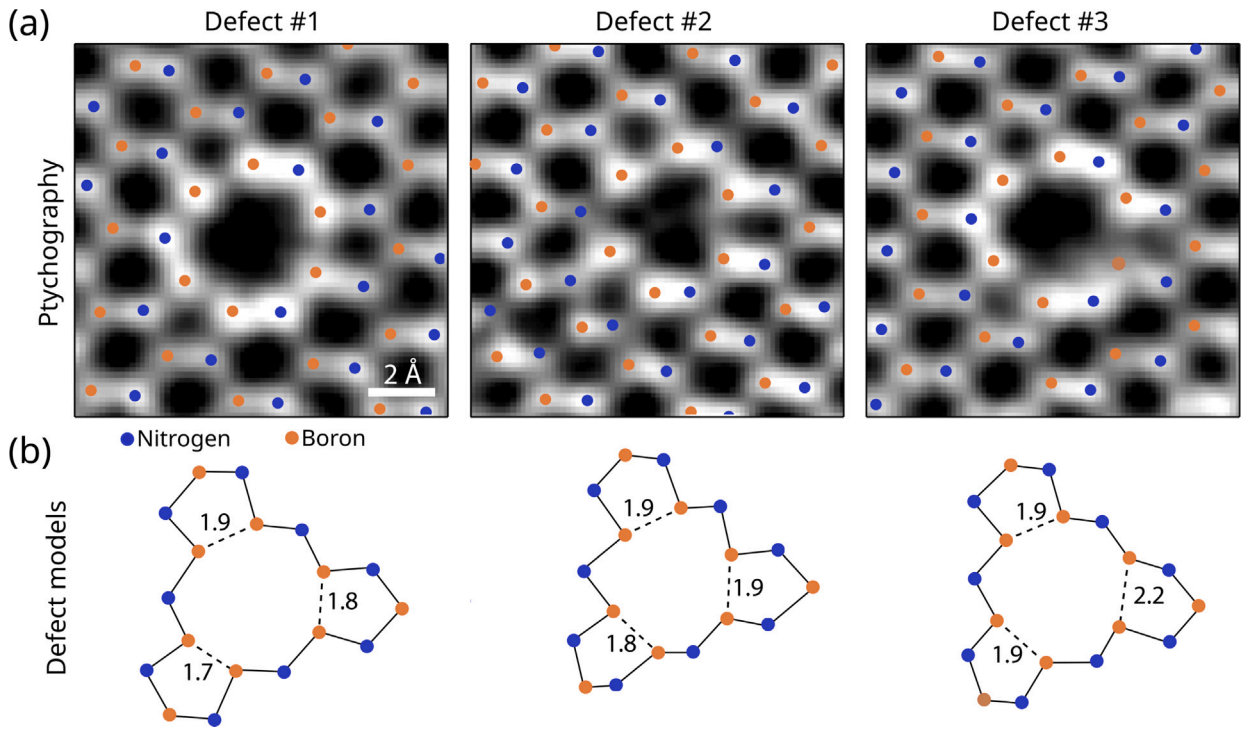

Fig. 3. (a) Ptychographic reconstructions of boron-terminated tetravacancies in monolayer hBN with atom map overlays. (b) Positions of the boron and nitrogen atoms around the defect edges as measured from the reconstructions. Dashed lines mark the B–B distances in the corner regions of the defects, measured in Ångström with a standard deviation of 0.1 Å.

Table 1
Literature review of vacancy defect shapes and edge terminations induced by electron irradiation of monolayer hBN in TEM and STEM for various operation parameters (beam voltage, sample temperature, dose rate, chamber vacuum level, etc.), including the results of the present work. Most studies report nitrogen termination, with boron and mixed terminations emerging in experiments performed at higher temperature or increased dose rate. Vacuum quality also appears to play a role. Other variables that could have an influence but are not addressed here include sample charging and surface contamination.

Defect shape	Edge termination	Mode	Voltage [kV]	Temperature [°C]	Additional parameters	References
Triangle	N	(S)TEM[a]	60/80/120	RT		[10,12–15]
Triangle	N	STEM	60	RT	O_2 atmosphere	[18]
Triangle	N	TEM	60	LN2		[15]
Triangle	N	TEM	30/60	400, 500		[15]
Triangle	B	STEM	60	RT	Higher dose rate, UHV	This work
Triangle	B	STEM	60/80	500		[14]
Hexagon	Mixed	TEM	80	RT	Higher dose rate	[17]
Hexagon	Mixed	TEM	30/60/80	700–1000, 1200		[15,16]
Parallelogram	Mixed	TEM	80	700–1000		[16]
Circular	Mixed	STEM	60	RT	UHV[b]	[18]
Circular	Mixed	TEM	60	800, 1000		[15]

[a] Z-contrast in STEM makes boron vs. nitrogen termination of the triangular defects straightforward to discern. This is not the case for TEM. Therefore, only those TEM results where the triangle edge terminations were confirmed by more detailed analysis are listed here.
[b] UHV base pressure in the sample chamber was an order of magnitude lower in [18] compared to the present work.

Upon increasing the temperature even further, vacancy defects of other shapes can form, namely hexagons [15,16], parallelograms [16], and approximately circular shapes [15]. Since these shapes exhibit alternating or mixed edge terminations, this suggests a regime where there is no longer a strong preference for the ejection of one element over the other. However, which of these non-triangular shapes is produced seems harder to predict, likely due to other varying parameters, such as the particular beam energy used, local charging of the hBN, residual species in the vacuum, and the electron dose rate.

In fact, in recent STEM experiments comparing room temperature defect growth in UHV vs. oxygen atmosphere, it was found that circular pores formed in UHV, whereas upon introducing oxygen, nitrogen-terminated triangles were produced [18]. Initially this result appears to be at odds with our own observation of triangular defects forming in UHV STEM. However, the vacuum level reported in [18] is an order of magnitude lower than ours, which could help account for the difference. A change in the energetics of pore growth depending on vacuum quality and partial pressure of oxygen has also been observed for graphene [41]. And in another room temperature study on hBN, this time in TEM mode, it was found that non-triangular defects, in this case hexagons, could be grown by increasing the electron dose rate [17]. Therefore, even at room temperature, the energetics of pore growth can be strongly influenced by other experimental parameters.

Placing the results of our study in the context of the existing literature, we thus propose that increasing the dose rate had an equivalent effect on the defect growth process as increasing the temperature to 500 °C did elsewhere [14]. That is, both increasing the dose rate and increasing the temperature can drive a transition from preferential

boron atom ejection to preferential nitrogen atom ejection, forming boron-terminated tetravacancies. Since we were operating at 60 kV, i.e. below the elastic knock-on threshold for ejection of atoms from the pristine lattice, damage due to inelastic effects will dominate [4]. In the case of hBN, this can also include charging [15], which can be expected to have a strong dependence on electron dose rate. Beam-mediated processes that preferentially consume nitrogen, involving chemical reactions with residual species in the vacuum or on the sample surface, can also play a role [14].

4. Conclusions

We have investigated the effect of 60 kV electron irradiation in STEM at low vs. high dose rate on the growth of vacancy defects in monolayer hBN. Over 60 datasets were analyzed to determine the dominant defect shapes and edge terminations. In low dose rate survey imaging, a mixture of triangular and hexagonal vacancy defect structures with varying edge termination was identified, whereas at higher dose rates, boron-terminated triangular defects were most commonly observed. Of the latter, boron-terminated tetravacancies were found to be the most stable. All experiments were performed in UHV with the samples held at room temperature. Contextualizing our findings within the existing literature, we conclude that preferential nitrogen atom ejection at the higher dose rates drives the formation of boron-terminated defects in a similar manner to increasing the sample temperature. In addition to Z-contrast in HAADF-STEM, we confirmed how near-edge structure in the boron K-edge can be used to assign boron termination. Finally, using 4D-STEM electron ptychography we detected a structural relaxation of the tetravacancies and revealed enhanced phase shift from the defect perimeters, likely hinting at charge redistribution at the defect edges to be studied in future work.

CRediT authorship contribution statement

Dana O. Byrne: Writing – review & editing, Writing – original draft, Visualization, Validation, Methodology, Investigation, Formal analysis, Data curation, Conceptualization. **Stephanie M. Ribet:** Writing – review & editing, Visualization, Validation, Investigation, Formal analysis, Data curation. **Demie Kepaptsoglou:** Writing – review & editing, Validation, Resources, Methodology, Investigation, Data curation. **Quentin M. Ramasse:** Writing – review & editing, Validation, Resources, Methodology, Investigation, Conceptualization. **Colin Ophus:** Writing – review & editing, Visualization, Validation, Supervision, Methodology, Investigation, Funding acquisition, Formal analysis. **Frances I. Allen:** Writing – review & editing, Writing – original draft, Validation, Supervision, Project administration, Methodology, Investigation, Funding acquisition, Formal analysis, Conceptualization.

Declaration of competing interest

The authors declare that they have no known competing financial interests or personal relationships that could have appeared to influence the work reported in this paper.

Acknowledgments

This work was funded in part by National Science Foundation Award No. 2110924. D.O.B. also acknowledges funding from the Department of Defense through the National Defense Science & Engineering Graduate (NDSEG) Fellowship Program. S.M.R. and C.O. acknowledge support from the U.S. Department of Energy Early Career Research Award program. SuperSTEM is the U.K. National Research Facility for Advanced Electron Microscopy, supported by the Engineering and Physical Sciences Research Council (EPSRC, UK) via grant numbers EP/W021080/1 and EP/V036432/1. The ion irradiation experiments were performed at the Biomolecular Nanotechnology Center, a core facility of the California Institute for Quantitative Biosciences. Work at the Molecular Foundry was supported by the Office of Science, Office of Basic Energy Sciences, of the U.S. Department of Energy under Contract No. DE-AC02-05CH11231. This research also used resources of the National Energy Research Scientific Computing Center (NERSC), a Department of Energy Office of Science User Facility using NERSC award BES-ERCAP0028035. The authors thank Juan Carlos Idrobo and Georgios Varnavides for helpful discussions.

Appendix A. Supplementary data

Supplementary material related to this article can be found online at https://doi.org/10.1016/j.ultramic.2025.114305.

Data availability

Data will be made available on request.

References

[1] Jannik C. Meyer, C. Kisielowski, R. Erni, Marta D. Rossell, M.F. Crommie, A. Zettl, Direct imaging of lattice atoms and topological defects in graphene membranes, Nano Lett. 8 (11) (2008) 3582–3586, http://dx.doi.org/10.1021/nl801386m.

[2] Ondrej L. Krivanek, Matthew F. Chisholm, Valeria Nicolosi, Timothy J. Pennycook, George J. Corbin, Niklas Dellby, Matthew F. Murfitt, Christopher S. Own, Zoltan S. Szilagyi, Mark P. Oxley, Sokrates T. Pantelides, Stephen J. Pennycook, Atom-by-atom structural and chemical analysis by annular dark-field electron microscopy, Nature 464 (7288) (2010) 571–574, http://dx.doi.org/10.1038/nature08879.

[3] Caglar O. Girit, Jannik C. Meyer, Rolf Erni, Marta D. Rossell, C. Kisielowski, Li Yang, Cheol-Hwan Park, M.F. Crommie, Marvin L. Cohen, Steven G. Louie, A. Zettl, Graphene at the edge: Stability and dynamics, Science 323 (5922) (2009) 1705–1708, http://dx.doi.org/10.1126/science.1166999.

[4] Toma Susi, Jannik C. Meyer, Jani Kotakoski, Quantifying transmission electron microscopy irradiation effects using two-dimensional materials, Nat. Rev. Phys. 1 (6) (2019) 397–405, http://dx.doi.org/10.1038/s42254-019-0058-y.

[5] Toma Susi, Demie Kepaptsoglou, Yung-Chang Lin, Quentin M. Ramasse, Jannik C. Meyer, Kazu Suenaga, Jani Kotakoski, Towards atomically precise manipulation of 2D nanostructures in the electron microscope, 2D Mater. 4 (4) (2017) 042004, http://dx.doi.org/10.1088/2053-1583/aa878f.

[6] Bethany M. Hudak, Jiaming Song, Hunter Sims, M. Claudia Troparevsky, Travis S. Humble, Sokrates T. Pantelides, Paul C. Snijders, Andrew R. Lupini, Directed atom-by-atom assembly of dopants in silicon, ACS Nano 12 (6) (2018) 5873–5879, http://dx.doi.org/10.1021/acsnano.8b02001.

[7] Cong Su, Mukesh Tripathi, Qing-Bo Yan, Zegao Wang, Zihan Zhang, Christoph Hofer, Haozhe Wang, Leonardo Basile, Gang Su, Mingdong Dong, Jannik C. Meyer, Jani Kotakoski, Jing Kong, Juan-Carlos Idrobo, Toma Susi, Ju Li, Engineering single-atom dynamics with electron irradiation, Sci. Adv. 5 (5) (2019) eaav2252, http://dx.doi.org/10.1126/sciadv.aav2252.

[8] Toma Susi, Identifying and manipulating single atoms with scanning transmission electron microscopy, Chem. Commun. 58 (88) (2022) 12274–12285, http://dx.doi.org/10.1039/d2cc04807h.

[9] Matthew G. Boebinger, Courtney Brea, Li-Ping Ding, Sudhajit Misra, Olugbenga Olunloyo, Yiling Yu, Kai Xiao, Andrew R. Lupini, Feng Ding, Guoxiang Hu, Panchapakesan Ganesh, Stephen Jesse, Raymond R. Unocic, The atomic drill bit: Precision controlled atomic fabrication of 2D materials, Adv. Mater. 35 (14) (2023) e2210116, http://dx.doi.org/10.1002/adma.202210116.

[10] Chuanhong Jin, Fang Lin, Kazu Suenaga, Sumio Iijima, Fabrication of a free-standing boron nitride single layer and its defect assignments, Phys. Rev. Lett. 102 (19) (2009) 195505, http://dx.doi.org/10.1103/PhysRevLett.102.195505.

[11] Jannik C. Meyer, Andrey Chuvilin, Gerardo Algara-Siller, Johannes Biskupek, Ute Kaiser, Selective sputtering and atomic resolution imaging of atomically thin boron nitride membranes, Nano Lett. 9 (7) (2009) 2683–2689, http://dx.doi.org/10.1021/nl9011497.

[12] Nasim Alem, Rolf Erni, Christian Kisielowski, Marta D. Rossell, Will Gannett, A. Zettl, Atomically thin hexagonal boron nitride probed by ultrahigh-resolution transmission electron microscopy, Phys. Rev. B Condens. Matter 80 (15) (2009) 155425, http://dx.doi.org/10.1103/PhysRevB.80.155425.

[13] Gyeong Hee Ryu, Hyo Ju Park, Junga Ryou, Jinwoo Park, Jongyeong Lee, Gwangwoo Kim, Hyeon Suk Shin, Christopher W. Bielawski, Rodney S. Ruoff, Suklyun Hong, Zonghoon Lee, Atomic-scale dynamics of triangular hole growth in monolayer hexagonal boron nitride under electron irradiation, Nanoscale 7 (24) (2015) 10600–10605, http://dx.doi.org/10.1039/c5nr01473e.

[14] Ovidiu Cretu, Yung Chang Lin, Masanori Koshino, Luiz H.G. Tizei, Zheng Liu, Kazutomo Suenaga, Structure and local chemical properties of boron-terminated tetravacancies in hexagonal boron nitride, Phys. Rev. Lett. 114 (7) (2015) http://dx.doi.org/10.1103/PhysRevLett.114.075502.

[15] Ovidiu Cretu, Yung-Chang Lin, Kazutomo Suenaga, Inelastic electron irradiation damage in hexagonal boron nitride, Micron 72 (2015) 21–27, http://dx.doi.org/10.1016/j.micron.2015.02.002.

[16] Thang Pham, Ashley L. Gibb, Zhenglu Li, S. Matt Gilbert, Chengyu Song, Steven G. Louie, Alex Zettl, Formation and dynamics of electron-irradiation-induced defects in hexagonal boron nitride at elevated temperatures, Nano Lett. 16 (11) (2016) 7142–7147, http://dx.doi.org/10.1021/acs.nanolett.6b03442.

[17] S. Matt Gilbert, Gabriel Dunn, Amin Azizi, Thang Pham, Brian Shevitski, Edgar Dimitrov, Stanley Liu, Shaul Aloni, Alex Zettl, Fabrication of subnanometer-precision nanopores in hexagonal boron nitride, Sci. Rep. 7 (1) (2017) 15096, http://dx.doi.org/10.1038/s41598-017-12684-x.

[18] Javed Umair, Langle Manuel, Zobac Vladimir, Markevich Alexander, Kofler Clara, Paul Martin, Mangler Clemens, Susi Toma, Kotakoski Jani, Origin of circular and triangular pores in electron-irradiated hexagonal boron nitride, 2025, arXiv:2507.13180.

[19] Yechan Noh, Alex Smolyanitsky, Stretch-inactivated ion transport through sub-nanoporous two-dimensional membranes, Phys. Rev. Mater. 8 (10) (2024) http://dx.doi.org/10.1103/physrevmaterials.8.l103001.

[20] Yechan Noh, Alex Smolyanitsky, Synaptic-like plasticity in 2D nanofluidic memristor from competitive bicationic transport, Sci. Adv. 10 (45) (2024) eadr1531, http://dx.doi.org/10.1126/sciadv.adr1531.

[21] Junjie Guo, Jaekwang Lee, Cristian I. Contescu, Nidia C. Gallego, Sokrates T. Pantelides, Stephen J. Pennycook, Bruce A. Moyer, Matthew F. Chisholm, Crown ethers in graphene, Nat. Commun. 5 (2014) 5389, http://dx.doi.org/10.1038/ncomms6389.

[22] Wu Zhou, Myron D. Kapetanakis, Micah P. Prange, Sokrates T. Pantelides, Stephen J. Pennycook, Juan-Carlos Idrobo, Direct determination of the chemical bonding of individual impurities in graphene, Phys. Rev. Lett. 109 (20) (2012) 206803, http://dx.doi.org/10.1103/PhysRevLett.109.206803.

[23] Quentin M. Ramasse, Che R. Seabourne, Despoina-Maria Kepaptsoglou, Recep Zan, Ursel Bangert, Andrew J. Scott, Probing the bonding and electronic structure of single atom dopants in graphene with electron energy loss spectroscopy, Nano Lett. 13 (10) (2013) 4989–4995, http://dx.doi.org/10.1021/nl304187e.

[24] Fredrik S. Hage, Myron D. Kapetanakis, Juan-Carlos Idrobo, Quentin M. Ramasse, Demie Kepaptsoglou, Atomic-scale spectroscopic imaging of the extreme-UV optical response of B- and N-doped graphene, Adv. Funct. Mater. 29 (52) (2019) 1901819, http://dx.doi.org/10.1002/adfm.201901819.

[25] F.S. Hage, G. Radtke, D.M. Kepaptsoglou, M. Lazzeri, Q.M. Ramasse, Single-atom vibrational spectroscopy in the scanning transmission electron microscope, Science 367 (6482) (2020) 1124–1127, http://dx.doi.org/10.1126/science.aba1136.

[26] Yi Jiang, Zhen Chen, Yimo Han, Pratiti Deb, Hui Gao, Saien Xie, Prafull Purohit, Mark W. Tate, Jiwoong Park, Sol M. Gruner, Veit Elser, David A. Muller, Electron ptychography of 2D materials to deep sub-ångström resolution, Nature 559 (7714) (2018) 343–349, http://dx.doi.org/10.1038/s41586-018-0298-5.

[27] Colin Ophus, Four-dimensional scanning transmission electron microscopy (4D-STEM): From scanning nanodiffraction to ptychography and beyond, Microsc. Microanal. 25 (3) (2019) 563–582, http://dx.doi.org/10.1017/S1431927619000497.

[28] Dana O. Byrne, Frances I. Allen, Atomic engineering of triangular nanopores in monolayer hBN for membrane applications: A decoupled seeding and growth approach, ACS Appl. Nano Mater. 8 (2025) 4565–4572, http://dx.doi.org/10.1021/acsanm.4c06998.

[29] Dana O. Byrne, Jim Ciston, Frances I. Allen, Probing defectivity beneath the hydrocarbon blanket in 2D hBN using TEM-EELS, Microsc. Microanal. 30 (4) (2024) 650–659, http://dx.doi.org/10.1093/mam/ozae064.

[30] Francisco de la Peña, et al., Hyperspy/hyperspy: V2.3.0, Zenodo, 2025, http://dx.doi.org/10.5281/zenodo.592838.

[31] Pauli Virtanen, Ralf Gommers, Travis E. Oliphant, Matt Haberland, Tyler Reddy, David Cournapeau, Evgeni Burovski, Pearu Peterson, Warren Weckesser, Jonathan Bright, Stéfan J. van der Walt, Matthew Brett, Joshua Wilson, K. Jarrod Millman, Nikolay Mayorov, Andrew R.J. Nelson, Eric Jones, Robert Kern, Eric Larson, C.J. Carey, İlhan Polat, Yu Feng, Eric W. Moore, Jake VanderPlas, Denis Laxalde, Josef Perktold, Robert Cimrman, Ian Henriksen, E.A. Quintero, Charles R. Harris, Anne M. Archibald, Antônio H. Ribeiro, Fabian Pedregosa, Paul van Mulbregt, SciPy 1.0 Contributors, SciPy 1.0: Fundamental algorithms for scientific computing in python, Nature Methods 17 (2020) 261–272, http://dx.doi.org/10.1038/s41592-019-0686-2.

[32] Benjamin H. Savitzky, Steven E. Zeltmann, Lauren A. Hughes, Hamish G. Brown, Shiteng Zhao, Philipp M. Pelz, Thomas C. Pekin, Edward S Barnard, Jennifer Donohue, Luis Rangel DaCosta, Ellis Kennedy, Yujun Xie, Matthew T. Janish, Matthew M. Schneider, Patrick Herring, Chirranjeevi Gopal, Abraham Anapolsky, Rohan Dhall, Karen C. Bustillo, Peter Ercius, Mary C. Scott, Jim Ciston, Andrew M. Minor, Colin Ophus, py4DSTEM: A software package for four-dimensional scanning transmission electron microscopy data analysis, Microsc. Microanal. 27 (4) (2021) 712–743, http://dx.doi.org/10.1017/S1431927621000477.

[33] Georgios Varnavides, Stephanie M. Ribet, Steven E. Zeltmann, Yue Yu, Benjamin H. Savitzky, Dana O. Byrne, Frances I. Allen, Vinayak P. Dravid, Mary C. Scott, Colin Ophus, Iterative phase retrieval algorithms for scanning transmission electron microscopy, 2023, arXiv:2309.05250v2.

[34] Anubhav Jain, Shyue Ping Ong, Geoffroy Hautier, Wei Chen, William Davidson Richards, Stephen Dacek, Shreyas Cholia, Dan Gunter, David Skinner, Gerbrand Ceder, Kristin A. Persson, Commentary: The materials project: A materials genome approach to accelerating materials innovation, APL Mater. 1 (1) (2013) http://dx.doi.org/10.1063/1.4812323.

[35] Hyoju Park, Yi Wen, Sylvia Xin Li, Woojin Choi, Gun-Do Lee, Michael Strano, Jamie H. Warner, Atomically precise control of carbon insertion into hBN monolayer point vacancies using a focused electron beam guide, Small 17 (23) (2021) e2100693, http://dx.doi.org/10.1002/smll.202100693.

[36] Chuang Gao, Lei Tao, Yu-Yang Zhang, Shixuan Du, Sokrates T. Pantelides, Juan Carlos Idrobo, Wu Zhou, Hong-Jun Gao, Spectroscopic signatures of edge states in hexagonal boron nitride, Nano Res. 12 (7) (2019) 1663–1667, http://dx.doi.org/10.1007/s12274-019-2417-5.

[37] R.F. Egerton, Limits to the spatial, energy and momentum resolution of electron energy-loss spectroscopy, Ultramicroscopy 107 (8) (2007) 575–586, http://dx.doi.org/10.1016/j.ultramic.2006.11.005.

[38] Kazu Suenaga, Haruka Kobayashi, Masanori Koshino, Core-level spectroscopy of point defects in single layer h-BN, Phys. Rev. Lett. 108 (7) (2012) 075501, http://dx.doi.org/10.1103/PhysRevLett.108.075501.

[39] Susumu Okada, Atomic configurations and energetics of vacancies in hexagonal boron nitride: First-principles total-energy calculations, Phys. Rev. B - Condens. Matter Mater. Phys. 80 (2009) http://dx.doi.org/10.1103/PhysRevB.80.161404.

[40] Christoph Hofer, Jacob Madsen, Toma Susi, Timothy J. Pennycook, Detecting charge transfer at defects in 2D materials with electron ptychography, J. Microsc. (2025) http://dx.doi.org/10.1111/jmi.13404.

[41] Gregor T. Leuthner, Toma Susi, Clemens Mangler, Jannik C. Meyer, Jani Kotakoski, Chemistry at graphene edges in the electron microscope, 2D Mater. 8 (3) (2021) 035023, http://dx.doi.org/10.1088/2053-1583/abf624.